Electronic Supplementary Information (ESI) for

A medicine-inspired hydroxyl-rich equimolar $ZnSO_4$/D-mannitol electrolyte enables horizontally stacked Zn deposition for long-cycling aqueous batteries

Jin Xiao,[#a] Chenbo Yuan,[#a] Cong Liu,[a] Ximei Sun,[a] Bing Cheng,[a] Zitong Huang,[a] Xiaowen Zhan,[a] Lingyun Zhu*[a]*

School of Materials Science and Engineering, Key Laboratory of Structure and Functional Regulation of Hybrid Materials of Ministry of Education, Anhui University, 230601 Hefei, Anhui, PR China

* Corresponding author; # Equal contributions
Email address: xiaowen.zhan@ahu.edu.cn (X.Z.); 22149@ahu.edu.cn (L.Z.)

Experimental Procedures

Electrolytes Preparation: 1 M $ZnSO_4$ electrolyte solution was prepared by dissolving 0.7189 g of $ZnSO_4 \cdot 7H_2O$ (99.995%, Aladdin) in 2.5 mL deionized water. The modified electrolytes (1M $ZnSO_4$ + x M D-Mannitol) were obtained by mixing D-Mannitol (≥99.0%, Maclin) with different concentrations (x= 0.01 M, 0.1 M, 0.5 M, 1 M and 2 M) into 1M $ZnSO_4$ solutions, denoted as 0.01-MNT, 0.1-MNT, 0.5-MNT, 1-MNT, 2-MNT. $ZnSO_4$ + MNT represents 1-MNT unless mentioned otherwise.

Synthesis of PANI@CC Cathode Materials: Typically, 0.365 mL of aniline (AR, Aladdin) was mixed with 15 mL of 1 M HCl drop by drop under continuous stirring in an ice bath at 0 °C. Then, several pieces of acid-treated carbon cloth (CC, WOS1011) with a radius of 6 mm were added to the above solution. After 1 h, 5 mL of 1 M HCl containing 0.228 g of ammonium persulfate (99.99%, Aladdin) was added into the mixed solution, followed by continuing stirring for one more hour. Finally, the PANI@CC was obtained after washing and drying at 60 °C in vacuum oven overnight.

***Electrochemical Measurements*:** CR2032 coin cells were assembled in an open-air environment to test the electrochemical properties. Electrochemical performances of Zn//Zn symmetric batteries, Zn//Ti asymmetric batteries, and Zn//PANI@CC full batteries were evaluated on a battery testing system (NEWARE CT-4008T). Zn foil (Φ 12 mm, 100 μm or 10 μm thickness), Ti mesh (Φ 12 mm, 1100 mesh, thickness: 0.3 mm), glass fiber separator (Whatman, GF/C), PANI@CC cathode and electrolytes were used for assembling coin cells. The coulombic efficiencies (CEs) were evaluated on Zn//Ti asymmetric batteries. Zn//PANI@CC full batteries were galvanostatically charged/discharged in the voltage range of 0.5–1.5 V at diverse current densities. Other electrochemical characterizations were carried out on the electrochemical workstation (Biologic VSP-300). Electrochemical impedance spectroscopy (EIS) was implemented from 1 Hz to 100 kHz. The potentiostatic chronoamperometry curves were measured at a fixed overpotential of −150 mV. Linear sweep voltammetry (LSV) curves were obtained with a scan rate of 5.0 mV s^{-1} by using Ti mesh as the work electrode, Zn foil as the counter electrode, and Ag/AgCl as the reference electrode, respectively. Tafel plots were measured by scanning between −0.895 V and −1.155

V at 1.0 mV s^{-1} with Zn foils as the working and counter electrodes, and Ag/AgCl as the reference electrode, respectively.

Characterizations: The morphologies and structures of the samples were characterized by Zeiss Crossbeam 550 SEM equipped with an energy dispersive X-ray spectroscopy (EDX) detector. The roughness and Young's modulus were tested by atomic force microscope (AFM, Dimension Icon, Bruker, USA) in peak-force tapping mode. The phase structures of samples were obtained by a SmartLab 9 KW Advance X-ray diffractometer (XRD). ^{2}H nuclear magnetic resonance (^{2}H NMR) spectroscopy were obtained from JNM–ECZ400S.The Raman spectra were obtained from Via–Reflex Raman spectrometer with a 532 nm excitation laser. The Fourier transform infrared (FTIR) spectra were obtained from Thermo Fisher Nicolet iS50. A DSA30 Drop Shape Analyzer was applied to analyze the wettability of the $ZnSO_4$ and $ZnSO_4$ + MNT electrolytes on Zn foils. The evolution of the Zn electrode interface during the constant current plating (1 mA cm^{-2}/1 mAh cm^{-2}) was monitored utilizing a GP-660v microscope. Cross-sectional morphologies were investigated using a JEOL JSM-7900F SEM equipped with EDX. Samples that cycled Zn anodes were prepared for BSE-EDX analysis by polishing with a JEOL IB-19520CCP cross-section polisher.

Molecular dynamics (MD) simulations: MD simulations of the electrolyte systems were conducted with the GROMACS 2023 simulation package. The all-atom optimized potential for liquid simulations (OPLS-AA) force field was applied, and parameters for H_2O, SO_4^{2-}, and D-mannitol in the OPLS-AA force field were established using the Ligpargen web server or the TTPMKTOP.[1-3] Molecular optimization of these compounds was performed at the B3LYP/6-31g(d, p) level in the Gaussian 16 package, incorporating the DFT-D3 (Becke-Johnson) method to consider van der Waals interactions before initiating simulations. Atomic charge distributions were determined using the restrained electrostatic potential 2 (RESP2) charge calculation through Gaussian and Multiwfn software for enhanced accuracy. Initial periodic models were generated using the PACKMOL package, and simulation boxes were set to dimensions of 3nm×3nm×3nm.[4] The MD simulation process comprised two-step energy minimization, two-step pre-equilibration, and a production simulation step. Evaluation of the final production simulation results utilized radial distribution function (RDF) and coordination structure counting methods. Visualizations of the MD simulations were conducted using the VESTA and VMD software.[5] The calculation of hydrogen

bonds is based on a geometric configuration where the distance between two oxygen atoms is less than 3.5 Å, and the O-H···O angle is less than 30°. In MD simulations, trajectory files of the system are generated, and then the analysis tool VMD is used to read these trajectory files frame by frame to identify atom pairs that meet the hydrogen bond criteria.

***Density functional theory (DFT) calculations*:** The Gaussian 16 package was employed for DFT calculations, utilizing Becke's three-parameter hybrid method with the Lee–Yang–Parr (B3LYP) correlation functional at the 6-31G (d, p) level.[6, 7] Additionally, the DFT-D3 (Becke-Johnson) method was considered to incorporate van der Waals interactions in these computations.[8] Following optimization and single-point calculations, Multiwfn and VMD software were utilized for visualizing the ESP results.[9, 10] The binding energy between A and B was determined using the following equation:

$$E_B = E_{complex} - E_{\mathrm{a}} - E_{\mathrm{b.}}$$

The adsorption energy calculations were based on the Perdew-Burke-Ernzerhof (PBE) formulation using DFT. We opted for projected augmented wave (PAW) potentials to accurately model the ionic cores and include valence electrons, employing a plane wave basis set with a kinetic energy cutoff of 450 eV.[11, 12] For the Kohn−Sham orbitals, we allowed partial occupancies using the Gaussian smearing method with a width of 0.05 eV. Self-consistency in electronic energy was achieved when the energy change fell below 10^{-5} eV, while geometry optimization was deemed convergent at an energy change below 0.02 eV $Å^{-1}$. To mitigate artificial interactions between periodic images, a 20 Å vacuum layer was routinely applied to the surface. Weak interactions were accounted for using the DFT+D3 method with empirical correction within Grimme's scheme.[8]

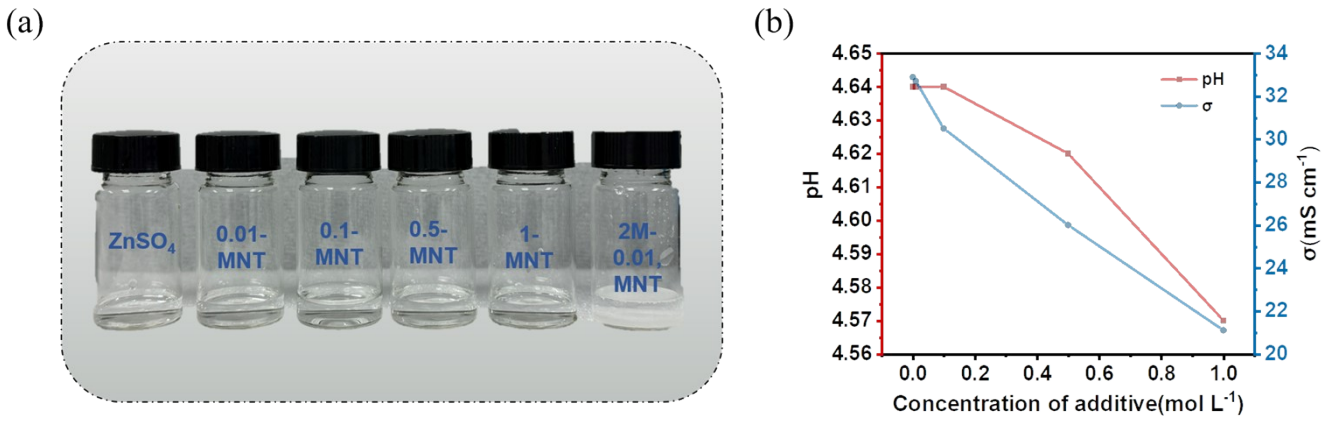

Figure S1. Optical images of 1 M $ZnSO_4$ electrolytes with various MNT concentrations (0, 0.01, 0.1, 0.5, 1, 2 M). (b) PH values and ion conductivity of the mixed electrolytes.

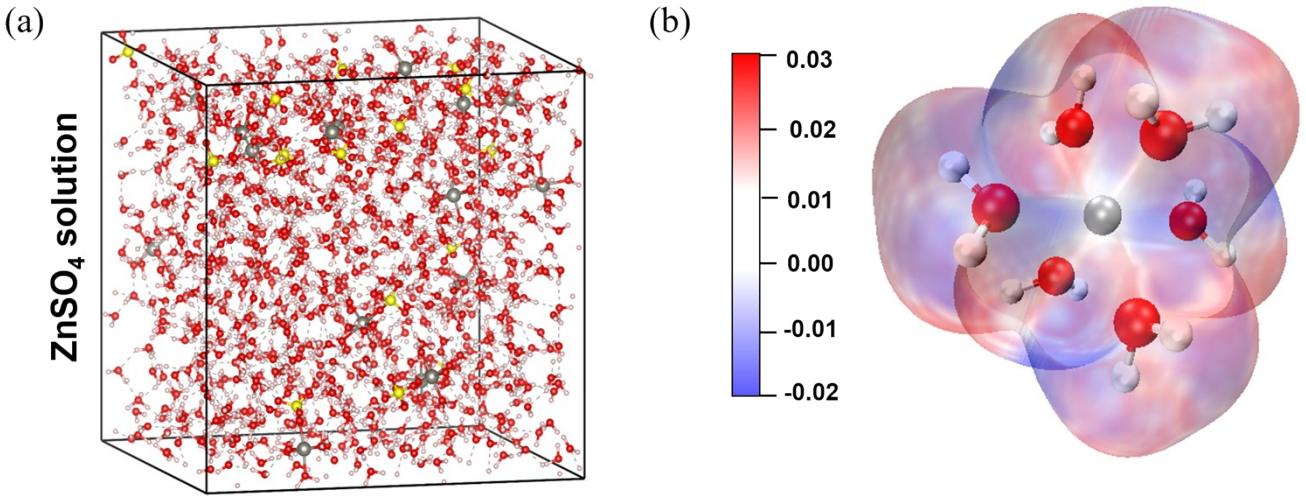

Figure S2. (a) Snapshot from MD simulation of the $ZnSO_4$ electrolyte. (b) ESP distribution of the $Zn(H_2O)_6]^{2+}$ solvation structure.

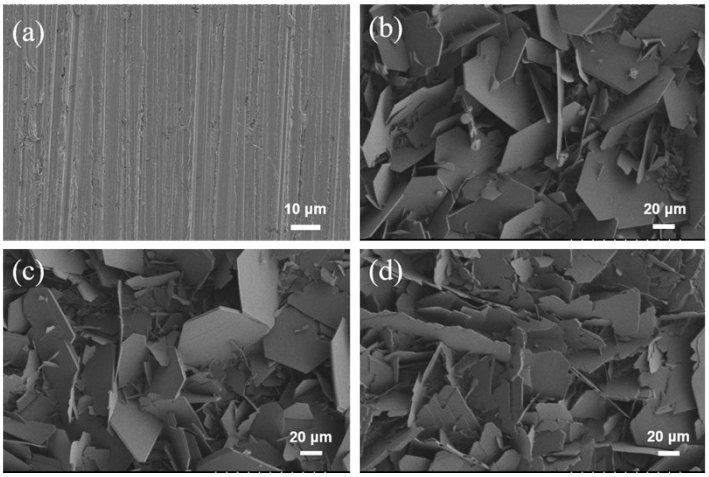

Figure S3. SEM images of (a) the polished Zn plate, and the Zn plates after soaking in (b) 0.01-MNT, (c) 0.1-MNT, (d) 0.5-MNT electrolytes for 5 days.

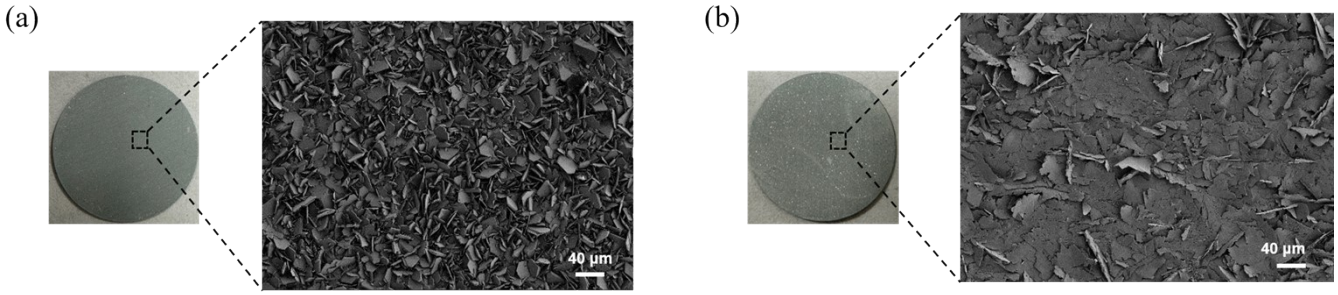

Figure S4. SEM images of the Zn plates after soaking in (a) $ZnSO_4$, (b) 1-MNT for 5 days.

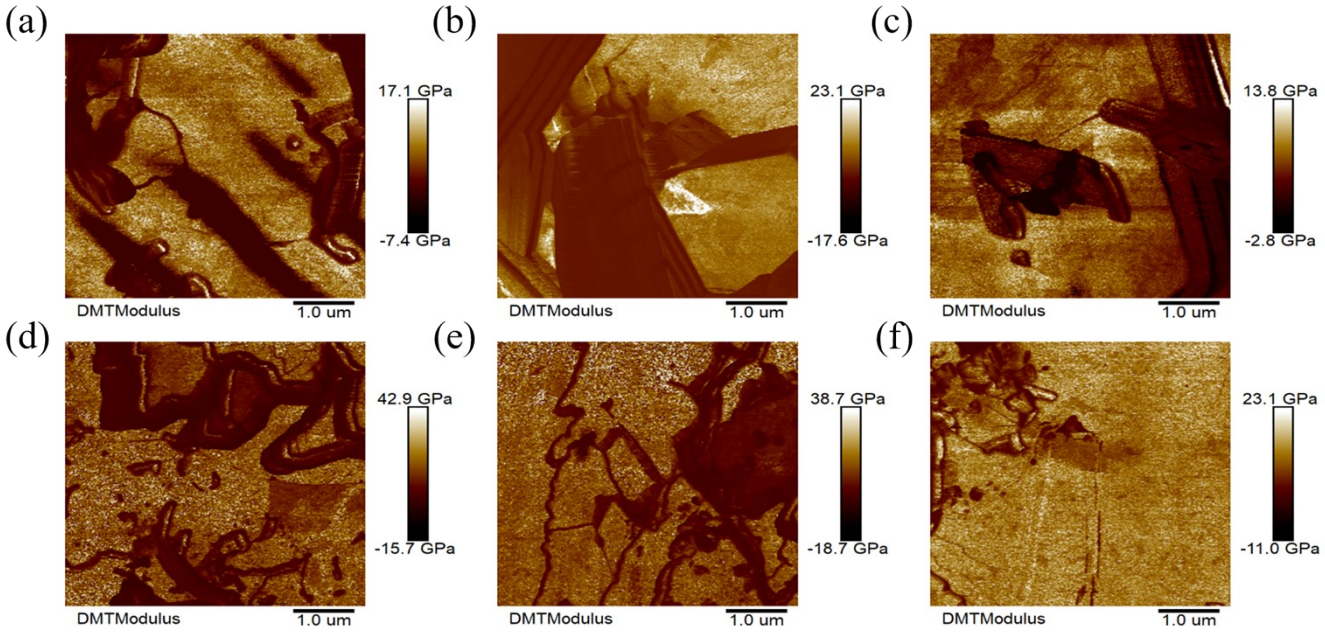

Figure S5. The Young' modulus maps of (a-c) $ZnSO_4$-Zn and (d-f) MNT-Zn measured by AFM.

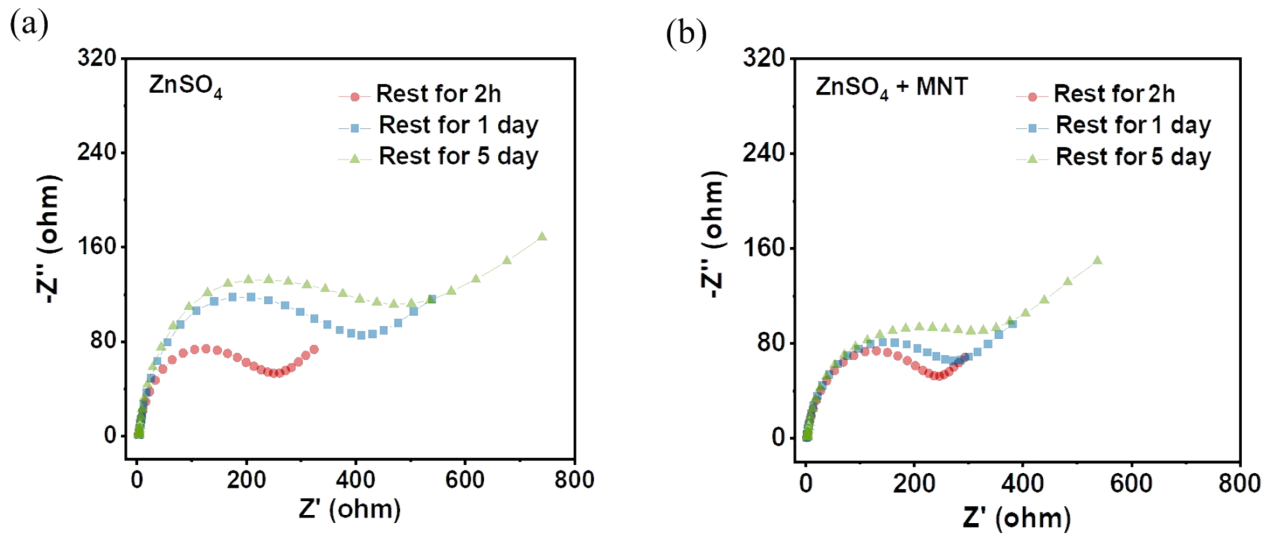

Figure S6. EIS spectra of the Zn symmetric cells in the $ZnSO_4$ and $ZnSO_4$ + MNT electrolytes after rest for 2 h, 1 day and 5 days.

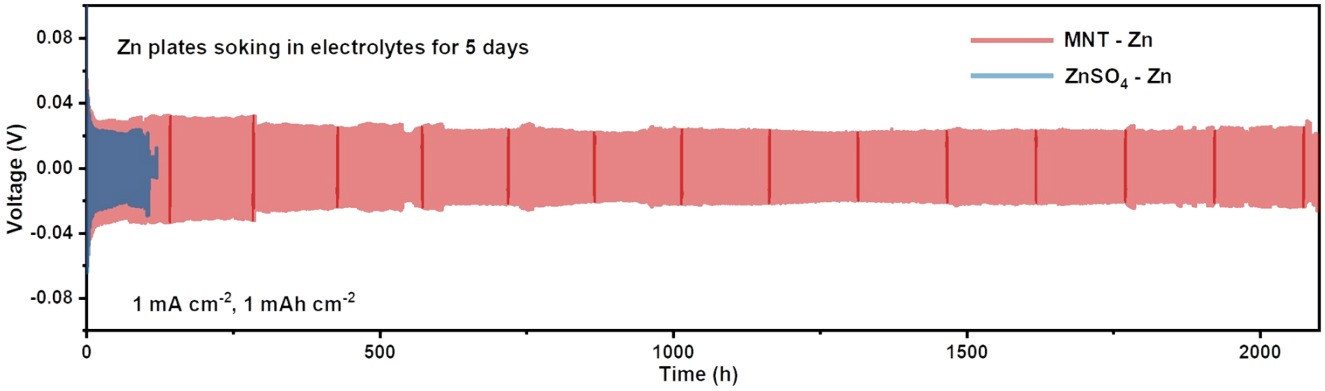

Figure S7. Cycling performances of the $ZnSO_4$-Zn//$ZnSO_4$-Zn and MNT-Zn//MNT-Zn symmetric cells with $ZnSO_4$ electrolyte at 1 mA cm^{-2} and 1 mAh cm^{-2}..

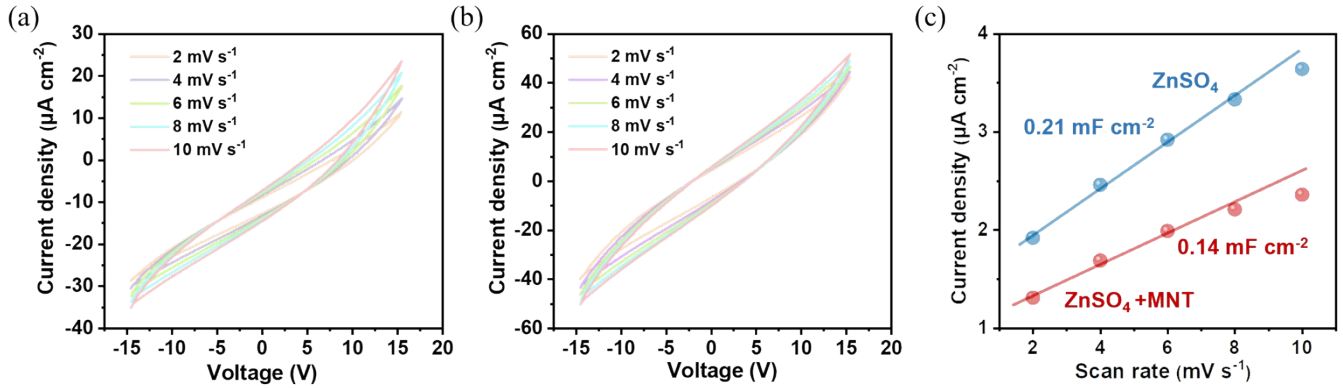

Figure S8. CV curves for Zn//Zn cells in the voltage range of 2 mV to 10 mV under various scanning rates in (a) $ZnSO_4$ and (b) $ZnSO_4$ + MNT electrolytes. (c) Plots of capacitive currents versus scan rates for the batteries.

Supplementary Note 1: The electric double-layer capacitance (C) was determined using the equation $C = i_c/v$, where C represents the capacitance, i_c denotes the double-layer current, and v signifies the scan rate. The linear relationship between i_c and v enables the estimation of capacitance. The capacitance is derived from the slope of the i_c versus v plots. i_c can be estimated as follows.

$$i_c = (i_{0v+} - i_{0v-})/2$$

The i_c value represents half of the difference in current observed between the forward and reverse scans at 0 V.

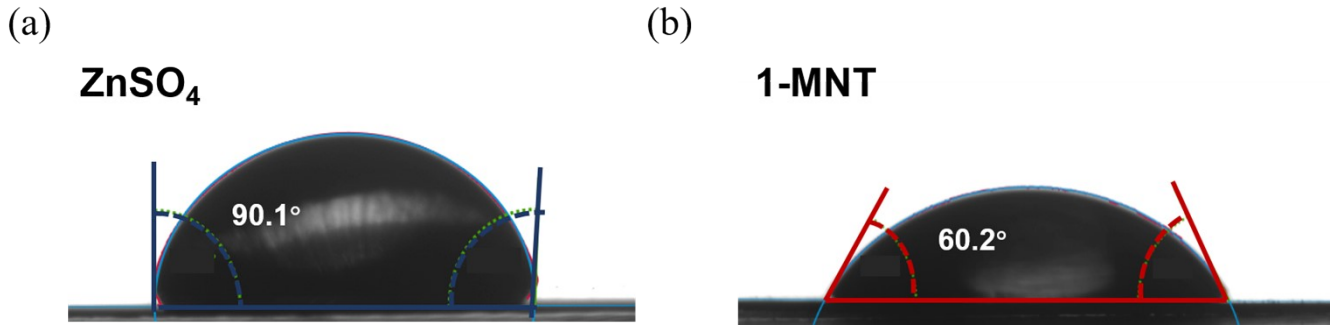

Figure S9. The contact angles of (a) $ZnSO_4$ and (b) $ZnSO_4$ + MNT electrolytes on Zn foil substrates.

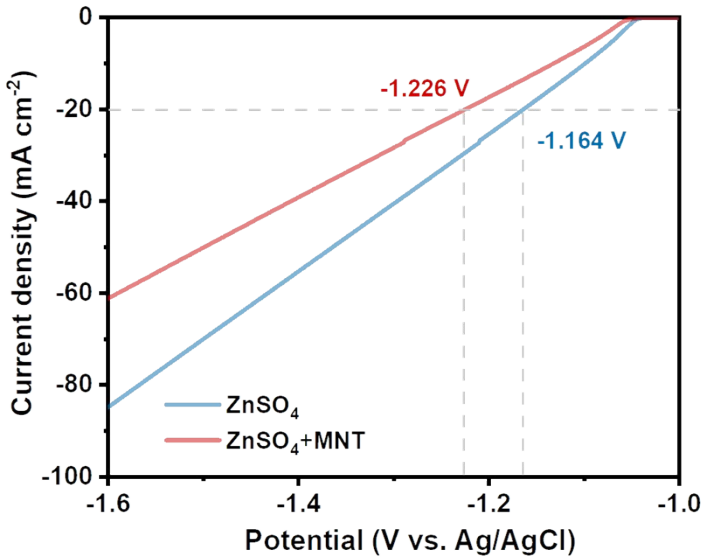

Figure S10. LSV of Zn electrodes in different electrolytes.

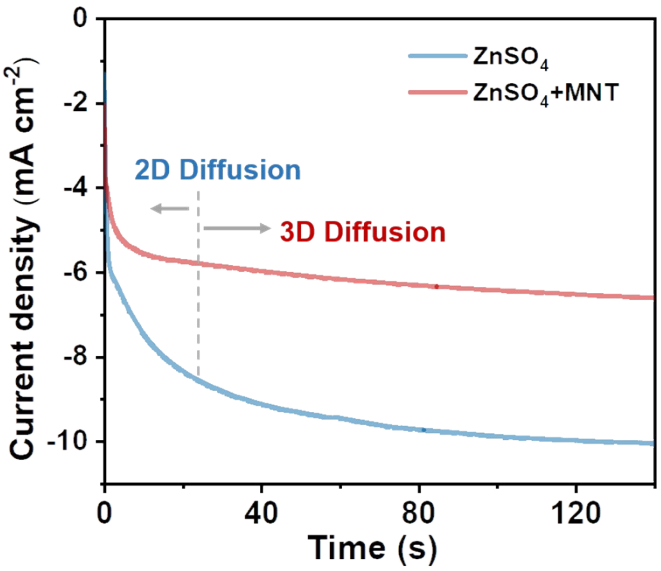

Figure S11. The CA curves of Zn electrodes measured in different electrolytes at a constant overpotential of −150 mV.

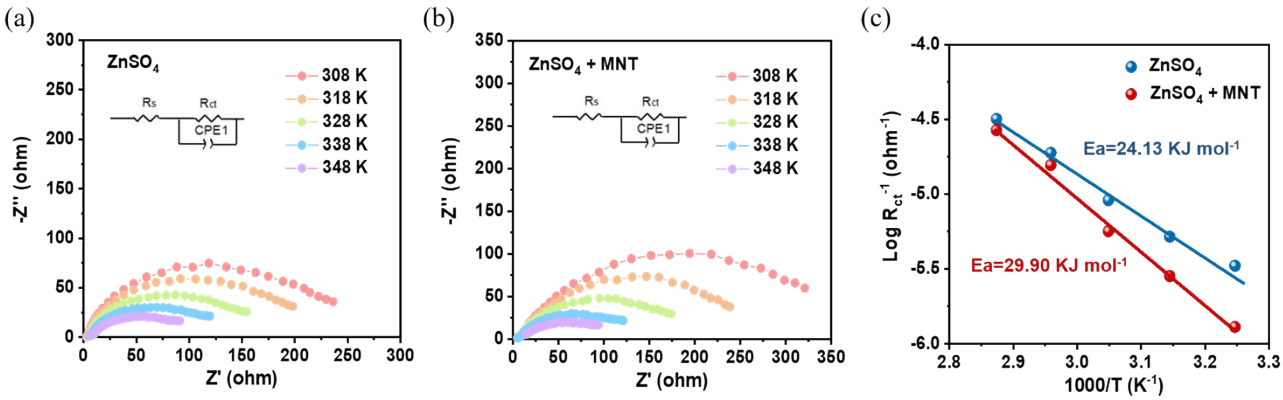

Figure S12. Nyquist plots of Zn//Zn symmetric cells tested at different temperatures using (a) $ZnSO_4$, (b) $ZnSO_4$ + MNT electrolytes. (c) Arrhenius curves and activation energies in $ZnSO_4$ and $ZnSO_4$ + MNT electrolytes.

Supplementary Note 2: the Arrhenius equation is shown below.

$$\frac{1}{Rct} = A_0 \exp\left(-\frac{Ea}{RT}\right)$$

where A_0 is a pre-exponential constant, and T, R, and E_a are the absolute temperature in Kelvin, the gas

constant, and the activation energy, respectively.

Table S1. The fitted Rct of Zn||Zn symmetric cells with $ZnSO_4$ and $ZnSO_4$ + MNT electrolyte at different temperatures.

R / T	308K	318K	328K	338K	348K
R ($ZnSO_4$)	239.6 Ω	197.2 Ω	154.5 Ω	112.6 Ω	89.8 Ω
R ($ZnSO_4$+MNT)	360.7 Ω	256.6 Ω	190.2 Ω	122.2 Ω	96.8 Ω

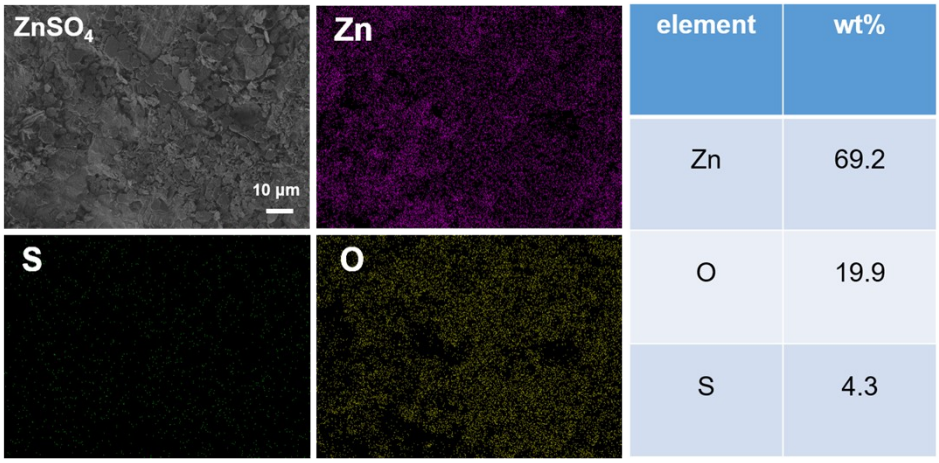

Figure S13. SEM and EDX mapping images of Zn anode cycled in $ZnSO_4$ electrolyte.

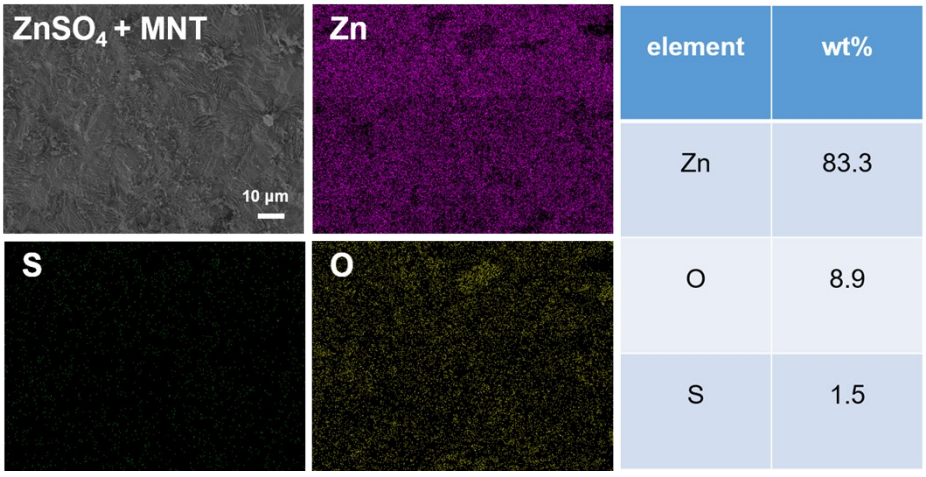

Figure S14. SEM and EDX mapping images of Zn anode cycled in $ZnSO_4$+ MNT electrolyte.

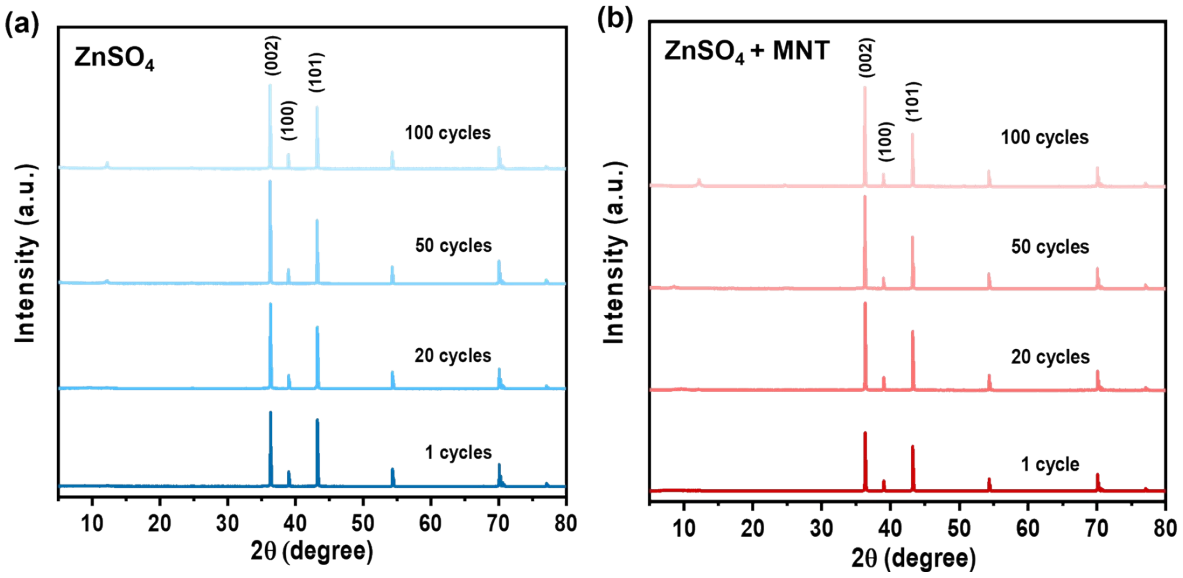

Figure S15. XRD patterns of the Zn surface after different cycles in $ZnSO_4$ and $ZnSO_4$ + MNT electrolytes.

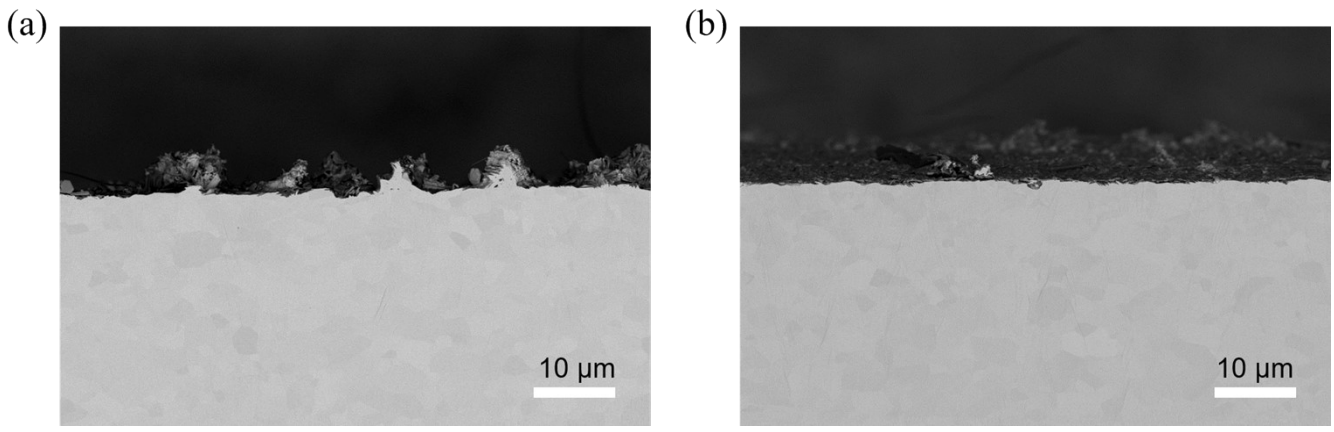

Figure S16. Cross-sectional BSE-SEM images of the cycled Zn after 100 cycles in (a) $ZnSO_4$ and (b) $ZnSO_4$ + MNT electrolytes at 1.0 mA cm^{-2}, 1.0 mAh cm^{-2}.

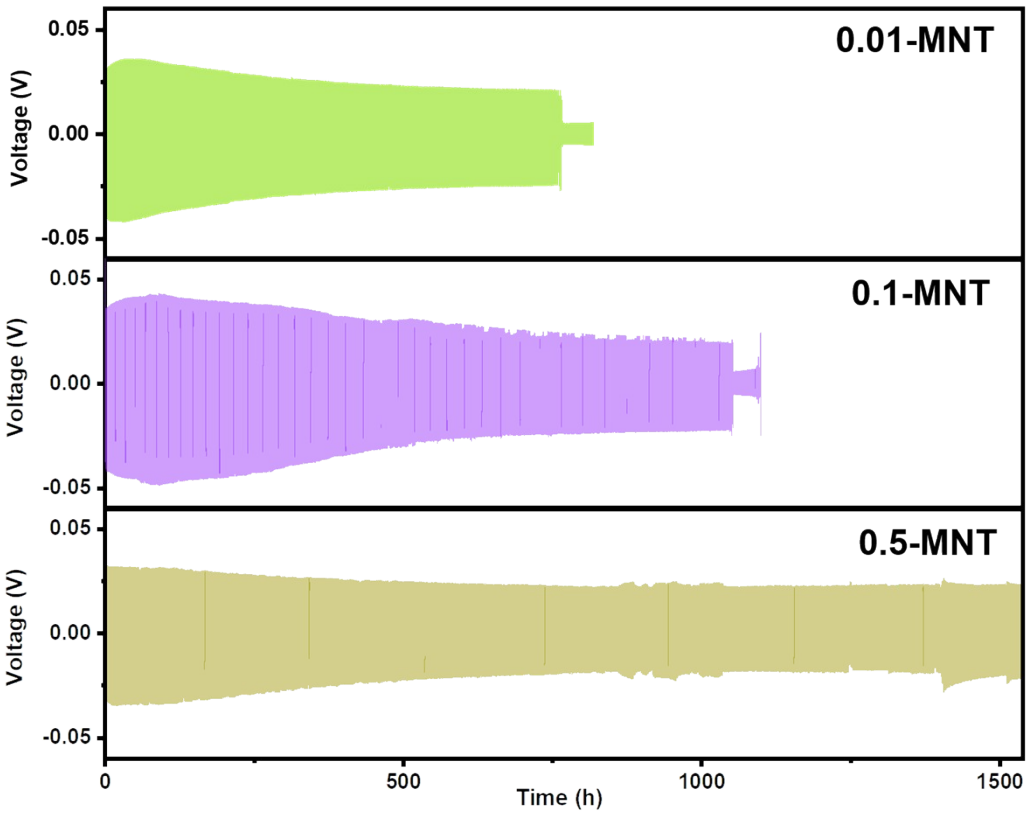

Figure S17. Cycling performances of Zn//Zn symmetric batteries tested in different electrolytes at 1 mA cm^{-2} and 1 mAh cm^{-2}.

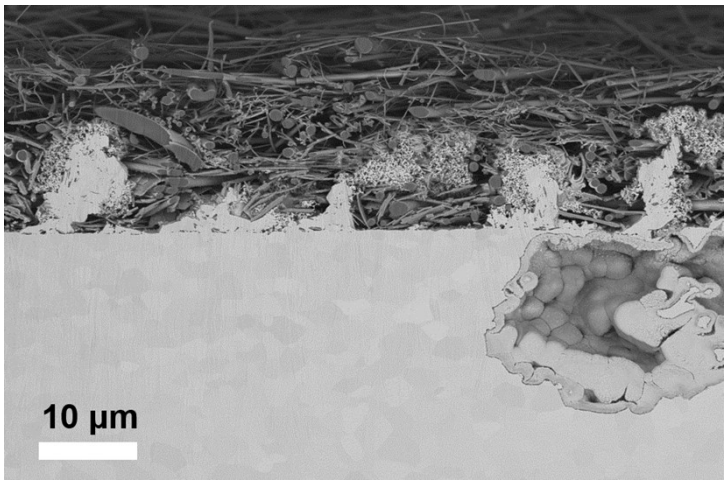

Figure S18. Cross-sectional BSE-SEM images of the cycled Zn (after 680 cycles) in $ZnSO_4$ electrolyte at 1.0 mA cm^{-2} and 1.0 mAh cm^{-2}.

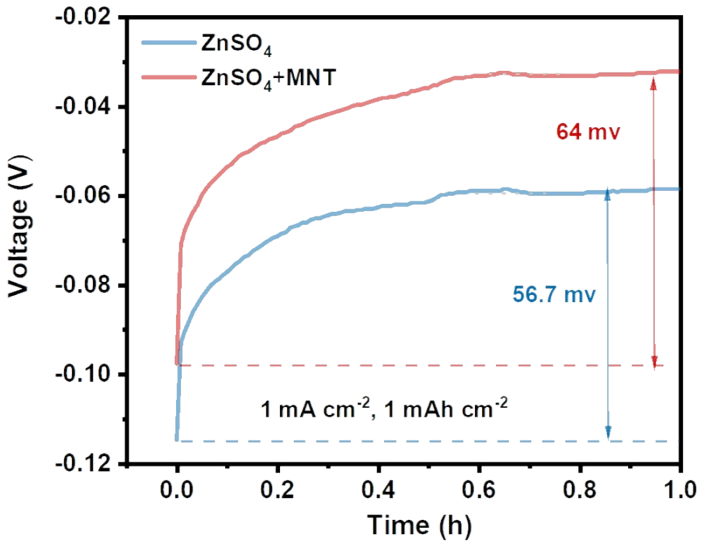

Figure S19. The nucleation overpotentials for Zn plating in different electrolytes.

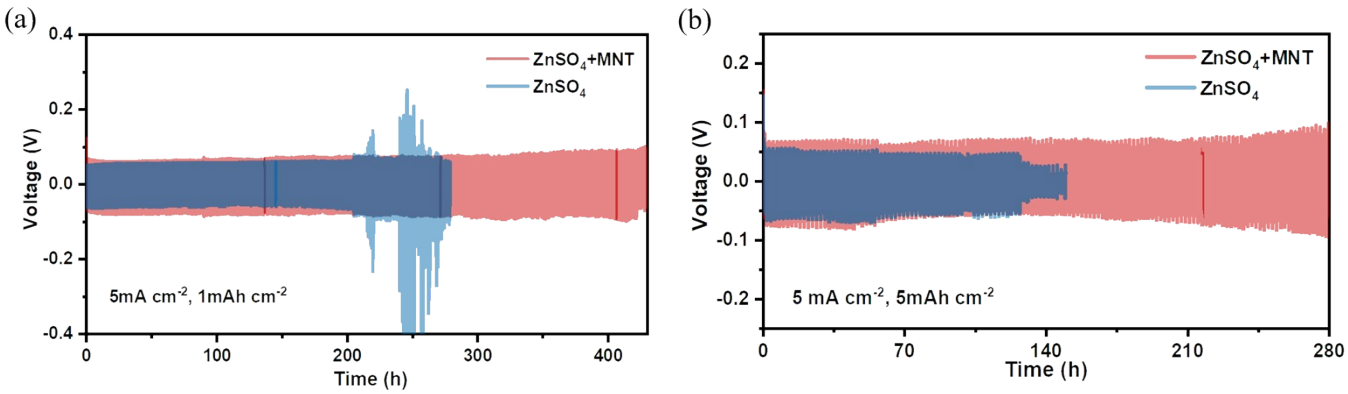

Figure S20. Long-term cycling stability of symmetrical cells at 5 mA cm^{-2} and 5 mAh cm^{-2}.

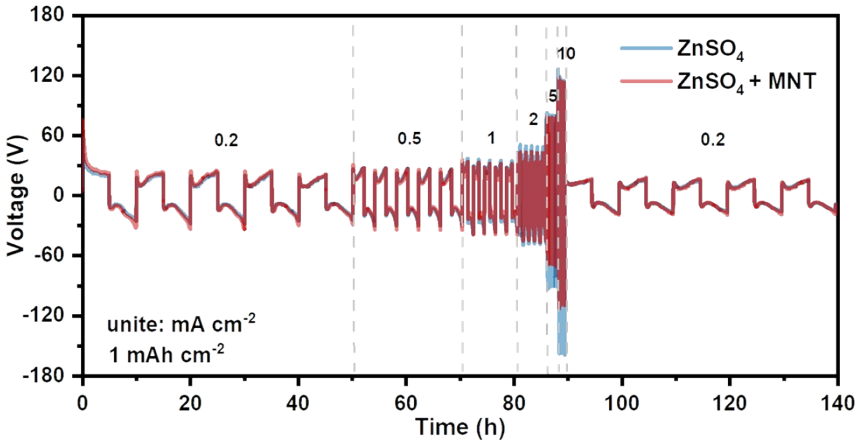

Figure S21. Rate performances of symmetrical cells at current densities from 0.2 to 10 mA cm^{-2}.

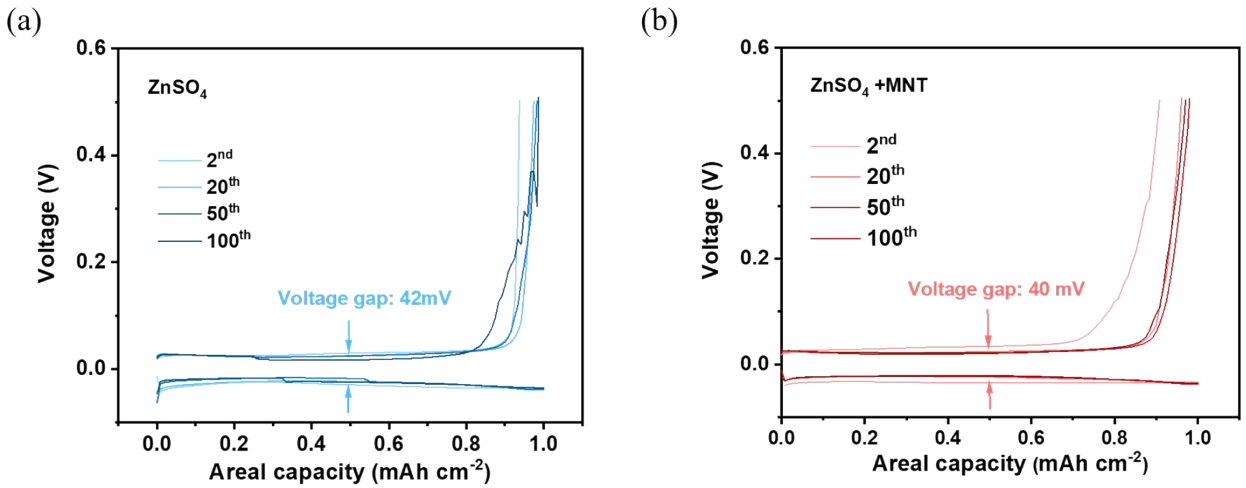

Figure S22. Voltage curves of the Zn plating/stripping processes for selected cycles.

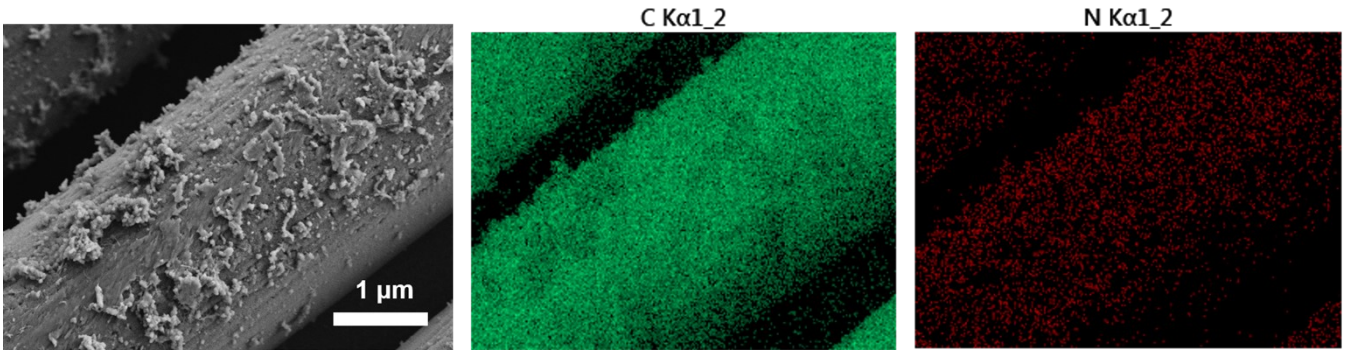

Figure S23. SEM and EDX mapping images of PANI@CC.

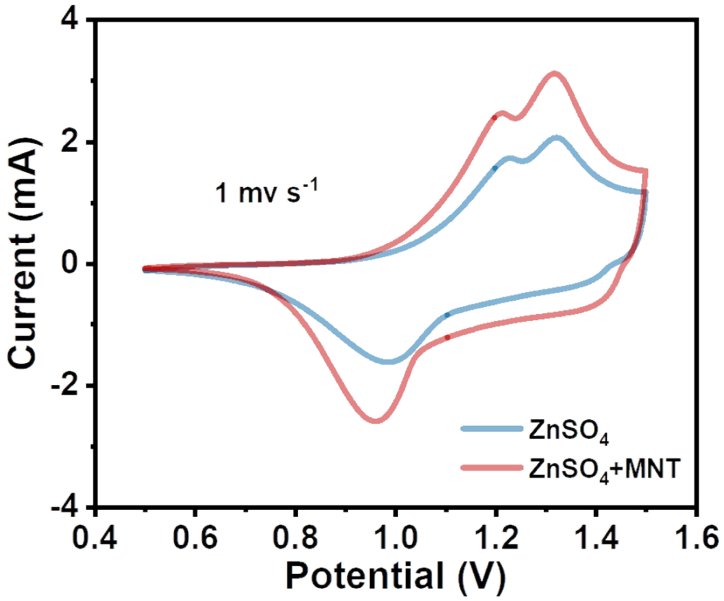

Figure S24. CV curves of Zn//PANI@CC full cells using different electrolytes.

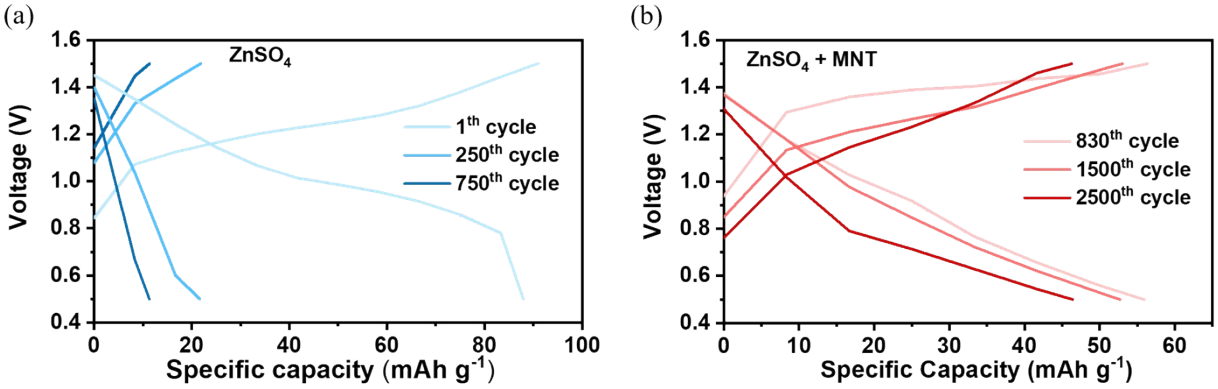

Figure S25. The voltage profiles of various cycles at 1 A g^{-1}.

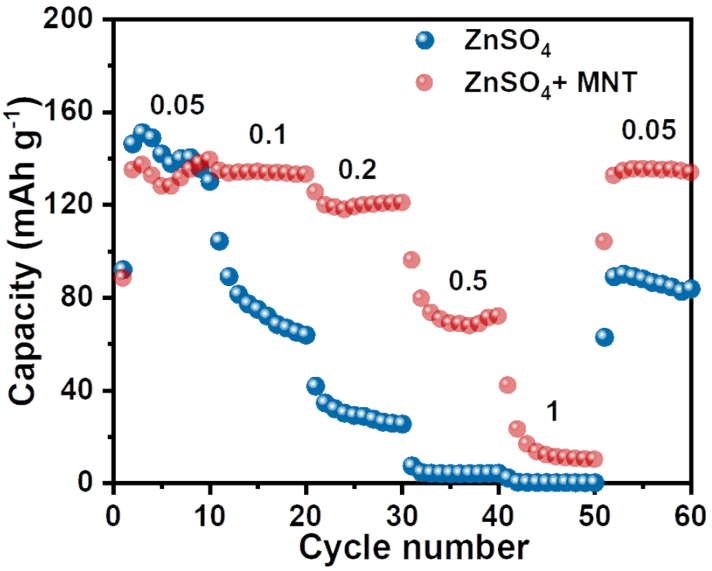

Figure S26. Rate capabilities of Zn//PANI@CC full cells different electrolytes at current densities from 0.05 to 1 A g^{-1}, respectively.

References

1. W.L. Jorgensen, J. Tirado-Rives, Proc. Natl. Acad. Sci. USA, 2005, **102**, 6665-6670.
2. W.L. Jorgensen, D.S. Maxwell, J. Tirado-Rives, J. Am. Chem. Soc. 1996, **118**, 11225-11236.
3. L.S. Dodda, J.Z. Vilseck, J. Tirado-Rives, W.L. Jorgensen, J. Phys. Chem. B, 2017, **121**, 3864-3870.
4. L. Martínez, R. Andrade, E.G. Birgin, J.M. Martínez, J. Comput. Chem. 2009, **30**, 2157-2164.
5. K. Momma, F. Izumi, J. Appl. Crystallogr. 2008, **41**, 653-658.
6. P.J. Stephens, F.J. Devlin, C.F. Chabalowski, M.J. Frisch, J. Phys. Chem. 1994, **98**, 11623-11627.
7. J. Tirado-Rives, W.L. Jorgensen, J. Chem. Theory and Comput. 2008, **4**, 297-306.
8. S. Grimme, J. Antony, S. Ehrlich, H. Krieg, J. Chem. Phys. 2010, **132**.
9. T. Lu, F. Chen, J. Comput. Chem. 2012, **33**, 580-592.
10. W. Humphrey, A. Dalke, K. Schulten, 1996, **14**, 33-38.
11. G. Kresse, D. Joubert, Phys. Rev. B, 1999, **59**, 1758-1775.
12. P.E. Blöchl, Phys. Rev. B, 1994, **50**, 17953-17979.